Cathodoluminescence mapping of electron concentration in MBE-grown GaAs:Te nanowires

Capucine Tong, Thomas Bidaud, Eero Koivusalo, Marcelo Rizzo Piton, Mircea Guina, Helder Galeti, Y Galvao Gobato, Andrea Cattoni, Teemu Hakkarainen, Stéphane Collin

▶ **To cite this version:**

Capucine Tong, Thomas Bidaud, Eero Koivusalo, Marcelo Rizzo Piton, Mircea Guina, et al.. Cathodoluminescence mapping of electron concentration in MBE-grown GaAs:Te nanowires. Nanotechnology, 2022, 10.1088/1361-6528/ac4d58 . hal-03539939

HAL Id: hal-03539939
https://hal.science/hal-03539939

Submitted on 22 Jan 2022

HAL is a multi-disciplinary open access archive for the deposit and dissemination of scientific research documents, whether they are published or not. The documents may come from teaching and research institutions in France or abroad, or from public or private research centers.

L'archive ouverte pluridisciplinaire **HAL**, est destinée au dépôt et à la diffusion de documents scientifiques de niveau recherche, publiés ou non, émanant des établissements d'enseignement et de recherche français ou étrangers, des laboratoires publics ou privés.

Cathodoluminescence mapping of electron concentration in MBE-grown GaAs:Te nanowires

Capucine Tong[1,2*], Thomas Bidaud[2*], Eero Koivusalo[3], Marcelo Rizzo Piton[3], Mircea Guina[3], Helder Vinicius Avano Galeti[4], Yara Galvo Gobato[5], Andrea Cattoni[1,2], Teemu Hakkarainen[3] and Stéphane Collin[1,2]

[*] *Authors contributed equally to this work.*

[1] Institut Photovoltaque dIle-de-France (IPVF), Palaiseau 91120, France

[2] Centre de Nanosciences et de Nanotechnologies (C2N), CNRS, Universit Paris-Saclay, 91120 Palaiseau, France

[3] Optoelectronics Research Centre, Physics Unit, Tampere University, Korkeakoulunkatu 3, 33720 Tampere, Finland

[4] Electrical Engineering Department, Federal University of So Carlos, 13565-905 So Carlos SP, Brazil

[5] Physics Department, Federal University of So Carlos, 13565-905 So Carlos SP, Brazil

E-mail: `stephane.collin@c2n.upsaclay.fr`

Abstract. Cathodoluminescence mapping is used as a contactless method to probe the electron concentration gradient of Te-doped GaAs nanowires. The room temperature and low temperature (10 K) cathodoluminescence analysis method previously developed for GaAs:Si is first validated on five GaAs:Te thin film samples, before extending it to the two GaAs:Te NW samples. We evidence an electron concentration gradient ranging from below 1 x 10^{18} cm^{-3} to 3.3 x 10^{18} cm^{-3} along the axis of a GaAs:Te nanowire grown at 640 C, and a homogeneous electron concentration of around 6 - 8 x 10^{17} cm^{-3} along the axis of a GaAs:Te nanowire grown at 620 C. The differences in the electron concentration levels and gradients between the two nanowires is attributed to different Te incorporation efficiencies by vapor-solid and vapor-liquid-solid processes.

Keywords: nanowires, GaAs, doping, cathodoluminescence

1. Introduction

One dimensional III-V semiconductor nanowires (NWs) are of great interest for many optoelectronic devices such as transistors [1], photodetectors [2], LEDs [3], photovoltaic devices [4] and other energy applications [5]. Their small diameter reduces the interface area with lattice-mismatched substrates, allowing them to be easily integrated to existing Si-based technologies. However, NWs small dimensions also induce a high dependence on their surface properties, rendering the control of carrier concentration necessary to avoid carrier depletion due to high density of surface states and form high quality p-n junctions [6, 7]. The growth of GaAs NWs is often carried out via the self-catalysed vapor-liquid-solid (VLS) growth mechanism in which impurity dopants are incorporated via the liquid Ga droplet or the NW sidewalls depending on the dopant flux and growth temperature [8–13]. Silicon is routinely used as n-type dopant in molecular beam epitaxy (MBE) grown GaAs planar layers [14, 15]. However, in GaAs NWs the well-known compensation effects resulting from the amphoteric nature of Si has so far hindered high-level n-type doping [16–18]. Tellurium (Te), as a group VI element, is a promising alternative to Si for n-type doping in GaAs NWs. Previous studies have already demonstrated the successful incorporation and activation of Te dopants in GaAs NWs using a combination of atom probe tomography, Raman spectroscopy, photoluminescence, secondary ion mass spectrometry, electron holography, single NW transport measurement and Kelvin probe force microscopy [19–22]. Electron concentrations up to the 10^{19} cm^{-3} range without compensation have been reported by Orr et al. [21], while more recently concentrations between 2 and 4 x 10^{19} cm^{-3} have also been reported for Te-doped GaAsSb NWs, using for the first time a combination of XPS/UPS and C-AFM/KPFM [23]. From the XPS spectra, signs of complex dopant distribution in the Te-doped GaAsSb NWs were observed but the latter could not be quantified using the above characterization techniques. Both axial and radial Te doping gradients were also observed by Hakkarainen et al. [22] in GaAs NWs. However, the limited spatial resolution of off-axis electron holography, standard Raman spectroscopy and single-nanowire transport characterization could again not allow the quantification of the carrier concentration gradient in the NWs. Spatially resolved Hall effect measurement in InP nanowires has been shown to allow the quantification of the carrier concentration variation in single NWs, which was found to be in agreement with carrier concentrations obtained from cathodoluminescence measurements on specific locations along these NWs [24,25]. Single NW Hall effect measurements however require the fabrication of nanoscale electrical contact which can be technically challenging and time-consuming.

In this work, cathodoluminescence mapping is used as a contactless method with nanoscale spatial resolution [26] to probe carrier concentration gradients in Te-doped GaAs NWs. First, we study five Te-doped GaAs thin films with electron concentrations between 5 x 10^{17} cm^{-3} and 1 x 10^{19} cm^{-3}, and we show that the method demonstrated for Si-doped GaAs [27,28] can be extended to Te-doped GaAs. Hence, at room temperature

the generalized Planck law and an absorption model are used to quantify the electron concentration. At low temperature, an empirical expression relating the CL peak full width at half maximum (FWHM) to the electron concentration is used. Then, we apply this carrier concentration assessment method to single NWs from two Te-doped GaAs NW samples grown at different temperatures. The carrier concentrations along the NW axis is determined with a spatial resolution down to 500 nm, and it is correlated with the temperature-dependent Te incorporation mechanisms.

2. Experimental Methods

2.1. Epitaxial growth

All samples are grown by solid source molecular beam epitaxy (MBE). The reactor is equipped with effusion cells for Ga and GaTe, and As is provided by a valved cracker. The As cracker is operated at 920 C to provide As_2 dimers. A series of planar 1 m thick Te-doped GaAs samples (Te-TF1 to Te-TF5, as labeled in Table 1) are grown on semi-insulating GaAs wafers to be used as a reference for the cathodoluminescence (CL) measurements and to act as Hall-measurement calibration samples for the GaTe cell temperatures. Two samples of self-catalysed GaAs NWs (Te-NW1 and Te-NW2) are grown on Si(111) substrates by using droplet-epitaxy mediated lithography-free oxide patterns as a template. Details of the template fabrication method are given in reference [29]. The NW growth is initiated by a 40 s Ga wetting followed by simultaneous opening of the GaTe shutter and As needle valve. The Ga flux corresponds to a 0.3 m/h planar (100) GaAs growth rate, and GaTe flux corresponds to 2 x 10^{19} cm^{-3} doping level on planar GaAs, as calibrated by Hall-measurements for the 0.3 m/h growth rate. The NW growth duration is 60 min. The NW growth is terminated by shutting all fluxes simultaneously and rapidly ramping down the substrate to preserve the Ga droplets.

Table 1. Epitaxial growth temperature (T_{growth}) and V/III ratio of the 5 reference thin film samples (Te-TFx) and the 2 nanowire samples (Te-NWx).

Sample Name	T_{growth} (C)	V/III ratio
Te-TF1	520	10
Te-TF2	521	10
Te-TF3	580	15
Te-TF4	520	11
Te-TF5	571	15
Te-NW1	640	9
Te-NW2	620	9

2.2. Characterization

Photoluminescence (PL) measurements are carried out at room temperature on all thin film samples. A 532 nm laser is used as an excitation source and the PL signal is detected using a spectrometer and a CCD array. After growth, NWs are dispersed on Si substrates for measurements in an Attolight Chronos cathodoluminescence microscope system. Luminescence is collected by an achromatic reflective objective (numerical aperture of 0.72). The acceleration voltage of the electron beam is set to 6 kV, and the probe current of 2 nA is kept constant within less than 5 %. As detailed in a previous work [27], in these excitation conditions the CL injection level ($< 10^{16}$ cm^{-3}) is expected to be more than one order of magnitude lower than the carrier concentrations studied. CASINO simulation shows that 75 % and 95 % of carriers are generated in a pear-shaped excitation volume within a radius/depth of approximately 30/95 nm and 110/185 nm, respectively. Luminescence spectra are dispersed with a diffraction grating (150 grooves/mm) in a Horiba iHR320 spectrometer and recorded with an Andor Newton charge-coupled device (CCD) camera (1024 256 pixel^2, pixel width 26 m). The corresponding spectral dispersion is 0.53 nm per pixel, and the image of a NW on the CCD (zero-order, no dispersion) is less than 3 pixels in length (NW length < 5 μm, magnification: 13), which results in a spectral resolution of about 2 nm. Luminescence spectra are corrected for the diffraction efficiency of the grating and the sensitivity of the CCD camera. The CL intensity spectra plotted in the following correspond to a spectral density of photon flux per unit of energy (counts.s^{-1}.eV^{-1}) [30]. The scale of the CL intensity maps correspond to a spectral density of photon flux integrated over all energies (counts.s^{-1}). Low temperature (LT) spectra are recorded for a sample holder set at 10 K. For GaAs thin film samples, room-temperature (RT) and LT CL spectra are averaged over hyperspectral maps (6464 pixel^2) measured over a 3131 μm^2 area. For sample Te-NW1, the RT CL hyperspectral map has been recorded with an integration time of 500 ms per pixel. To limit the image drift, the exposure time has been reduced for Te-NW2 down to 50 ms for the RT CL hyperspectral map, and 25 ms for the LT map. The narrow length distribution witnessed in similarly grown NWs [31] strongly suggests that the dopant incorporation is uniform from NW to NW. For each NW sample presented in this article, 3 NWs were measured and similar results were obtained. Transmission electron microscopy (TEM) images were acquired on other representative NWs from both Te-NW1 and Te-NW2 samples, see Figures A2 and A3 in Appendix.

3. Electron Concentration Determination in GaAs:Te Thin Film References

Chen et al. [27, 28] have developed a method to assess quantitatively the electron concentration in Si-doped GaAs using cathodoluminescence. In the following, we extend this work to five Te-doped GaAs thin films with different doping concentrations (growth parameters summarized in Table 1). Their luminescence spectra are measured at room

and low temperature, and used to confirm the consistency between Te-doped and Si-doped results.

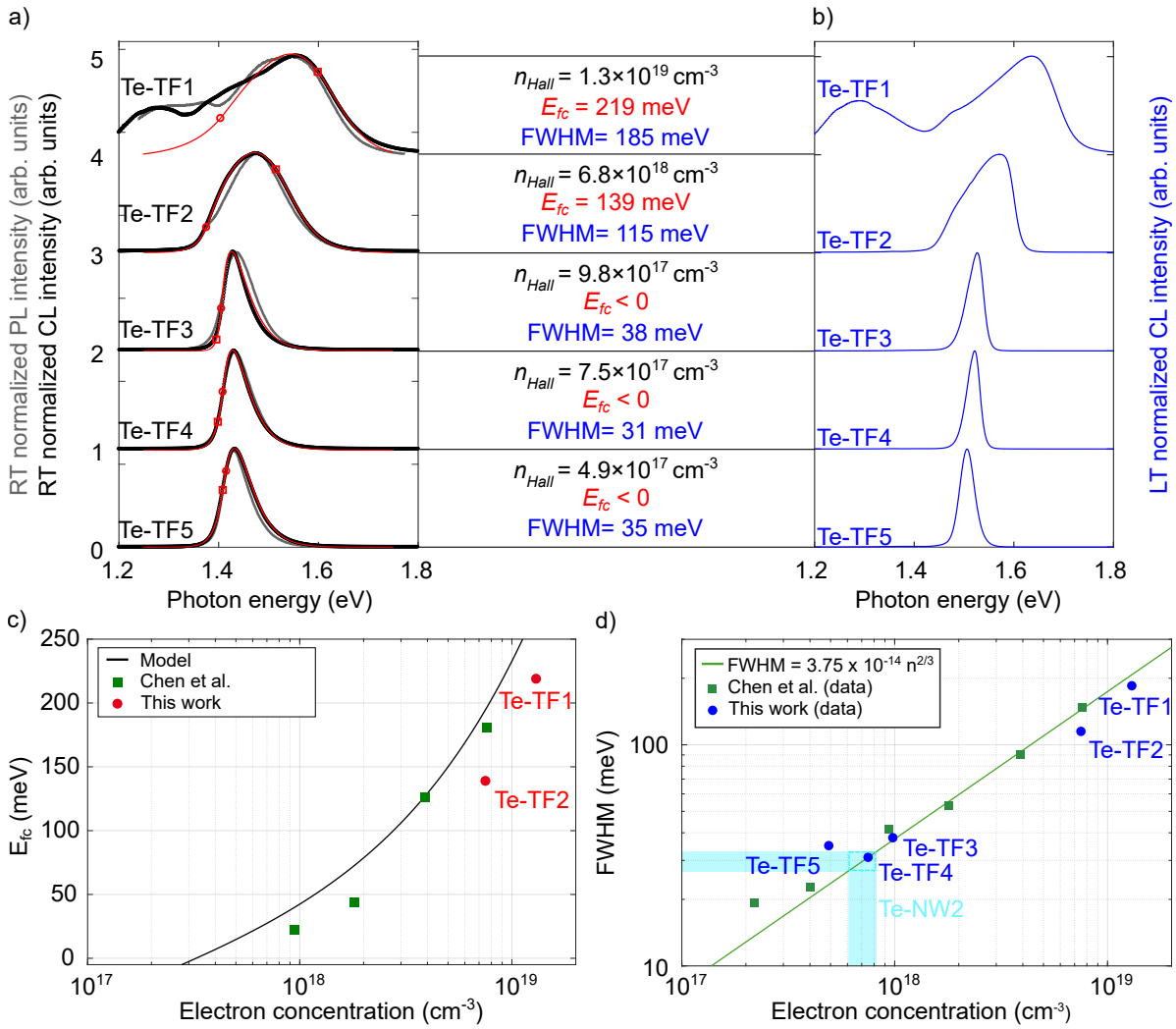

Figure 1. (a) Room temperature PL (grey) and CL (black) spectra of GaAs:Te thin films, and the fits of CL spectra (red). Red circles and squares correspond to the fitted bandgaps (E_g) and electron Fermi levels (E_{fc}), respectively. (b) Low temperature (10 K) CL spectra of the same samples. The Hall doping (n_{Hall}), E_{fc} and FWHM measured at LT are reported. (c) Electron Fermi levels (with E_C as a zero reference) extracted from RT CL spectra fits (red) are compared to values obtained on Si-doped GaAs thin films [27] (green) and a theoretical model accounting for the non-parabolicity of the conduction band [27, 32, 33] (solid curve). (d) FWHM extracted from LT CL spectra of the thin film samples as a function of the electron concentration (n_{Hall}). The green solid line is the relation derived by Chen et al. [27] from Si-doped GaAs thin film samples. It is used to determine the electron concentration in Te-NW2 (light blue region). All electron concentrations (n_{Hall}) in this figure were determined using Hall effect measurements.

Figure 1a shows the RT PL (grey) and CL (black) spectra of the five GaAs:Te thin film samples from Table 1. Figure 1b shows their LT CL spectra (blue). The carrier concentration (n_{Hall}) of each sample is determined using Hall effect measurements. The

red curves correspond to the fits of the CL spectra obtained using the generalized Planck law as described in references [27] and [30]. The fitted band gap (E_g) and electron Fermi level (E_{fc}) are indicated on the fits with circles and squares, respectively. All the RT and LT CL spectra exhibit a distinct peak corresponding to GaAs band-to-band emission. A clear blueshift and broadening of this peak at both RT and LT can be observed with increasing electron concentration, as expected from conduction band filling (Burstein-Moss effect) [34, 35] and indirect recombinations between free electrons and localized holes acting as acceptor-like states [36]. Sample Te-TF2 presents a low-energy shoulder on the GaAs emission peak, which is even more pronounced in Te-TF1 and has been previously attributed to donor-acceptor pair luminescence coming from the substrate region [36]. Sample Te-TF1 also presents a distinct CL peak around 1.28 eV which has been previously attributed to sub-bandgap states [30]. Finally, a good correlation can be observed between the RT CL and PL spectra from Figure 1a. The small discrepancies between PL and CL at energies below the bandgap (sample Te-TF1) come from the higher injection level of CL which may partly saturate the defects.

The E_{fc} values obtained (with the bottom of the conduction band (E_C) as zero-energy reference) from the RT CL spectra of samples Te-TF1 and Te-TF2 are plotted in Figure 1c and compared to the electron Fermi levels obtained previously from Si-doped GaAs thin film samples (green) [27], as well as to a theoretical model (solid curve) relating the electron Fermi level to the electron concentration [32, 33]. The model assumes a conduction band effective density of states of N_C = 4.2 x 10^{17} cm^{-3} [36, 37] and accounts for the non-parabolicity of the conduction band. Like the Si-doped GaAs thin film samples, the data from Te-doped GaAs samples correlate well to the theoretical model. However, the E_{fc} values from this study are slightly lower than the ones from Si-doped GaAs samples. This could be explained by bandgap shrinkage due to non-negligible electron occupation in CB tail states [36], surface depletion in GaAs or reabsorption effect [27]. Since the conduction band only starts to be filled above a doping concentration of 5 x 10^{17} cm^{-3} in GaAs [34,35], the electron Fermi level cannot be determined below this doping concentration. Between 5 x 10^{17} cm^{-3} and 1 x 10^{18} cm^{-3}, the E_{fc} still cannot be accurately determined, which is why Te-TF3, Te-TF4 and Te-TF5 do not appear in Figure 1c and their electron Fermi level is indicated as negative in Figure 1a. Nevertheless, the results obtained in this study are consistent with previous results from Si-doped GaAs [27] above 1 x 10^{18} cm^{-3}. Figure 1d compares the FWHM values extracted from the LT CL spectra of the thin film samples (dark blue) to the relation (green) obtained by Chen et al. [27] from Si-doped GaAs thin film samples, relating the peak FWHM to the electron concentration (n) in cm^{-3}:

$$FWHM(eV) = 3.75 \times 10^{-14} \times n^{2/3} \quad (1)$$

This relation enables the determination of doping concentrations between 4 x 10^{17} cm^{-3} and 1 x 10^{19} cm^{-3}. The LT FWHM values obtained from the Te-doped GaAs thin film samples are in very good agreement with this model.

Overall, both the RT and LT cathodoluminescence-based methods developed by

Table 2. Summary of the carrier concentrations of GaAs:Te thin films obtained from CL spectra at RT and LT (10K), compared to values obtained from Hall effect measurements at RT.

Sample	Carrier concentration CL from E_{fc} (RT) (cm^{-3})	Carrier concentration CL from FWHM (LT) (cm^{-3})	Carrier concentration Hall effect (RT) (cm^{-3})
Te-TF1	9.1 x 10^{18}	1.1 x 10^{19}	1.3 x 10^{19}
Te-TF2	4.5 x 10^{18}	5.4 x 10^{18}	6.8 x 10^{18}
Te-TF3	$<$ 1 x 10^{18}	1 x 10^{18}	9.8 x 10^{17}
Te-TF4	$<$ 1 x 10^{18}	7.5 x 10^{17}	7.5 x 10^{17}
Te-TF5	$<$ 1 x 10^{18}	8.6 x 10^{17}	4.9 x 10^{17}

Chen et al. [27] for determining carrier concentrations in Si-doped GaAs can also provide an assessment of the electron concentration in Te-doped GaAs, with an accuracy comparable to Hall effect measurements. The results deduced from E_{fc} and FWHM applied to the reference models are summarized in Table 2. The RT and LT methods allow for the determination of electron concentrations above 1 x 10^{18} cm^{-3} and above 4 x 10^{17} cm^{-3}, respectively. These methods will be used in the next sections to determine the electron concentrations in single NWs from two Te-doped GaAs samples.

4. Electron concentration mapping in GaAs:Te NWs

The two NW samples, Te-NW1 and Te-NW2, differ in growth temperatures (640 C and 620 C respectively). SEM analysis (Appendix A1 and ref [22]) shows that the NWs in Te-NW1 are on average 3700 nm long and have a uniform diameter of 170 nm throughout their length, whereas NWs in Te-NW2 are longer (4950 nm) and tapered with a bottom diameter of 220 nm and a top diameter of 160 nm. HR-TEM analysis (Figures A2 and A3 in Appendix) reveals that both NWs have predominantly zinc blende (ZB) crystal structure with frequent twinning. In Te-NW1 the twinning increases towards the NW tip, where twinning superlattices are witnessed, whereas in Te-NW2, the most frequent twinning is found in the middle section of the NW. The tip region of Te-NW2 shows stacking faults and polytypism which evolve into longer wurtzite (WZ) segments followed by a segment with mixed crystal phase and finally short ZB segment right below the droplet. Such microstructure can be explained by a gradual decrease of the droplet contact angle caused by lower As evaporation rate at the lower growth temperature. [38]. Thus, based on the NW dimensions and the microstructure, we can conclude that Te-NW2 was grown with a higher supersaturation than Te-NW1.

Single NWs from the two NW samples described above are characterized using cathodoluminescence mapping in conditions similar to that of the thin film samples. Due to a small drift attributed to charge effects during the CL measurement of Te-NW1, the hyperspectral images shown in Figure 2b-d are drift corrected by 1 pixel (areas 1, 2 and 3 only).

4.1. NWs grown at 640 C (Te-NW1)

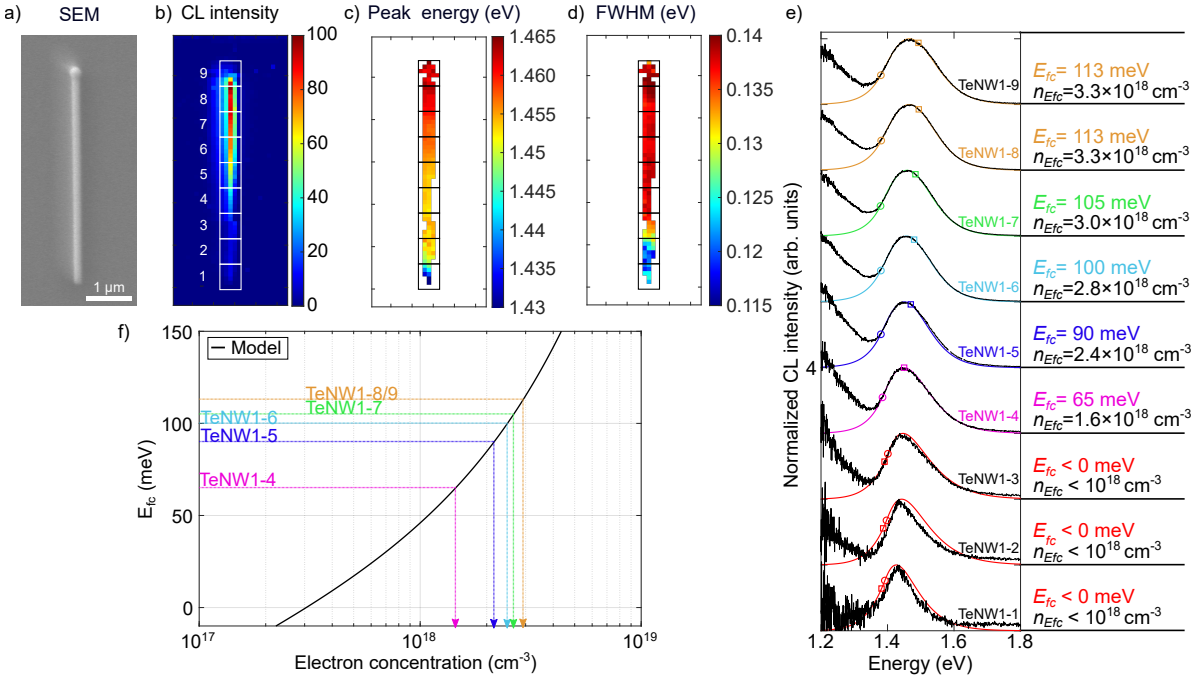

Figure 2. A single NW from sample Te-NW1 studied by RT cathodoluminescence. (a) SEM image, (b) RT panchromatic CL intensity map, (c) CL peak energy map and (d) FWHM map (27 x 64 pixel^2). (e) CL spectra averaged over the 9 different areas (5 x 6 pixel^2 each) shown in (b), and their respective fits with a generalized Planck law (coloured curves). Circles and squares correspond to the fitted bandgaps and electron Fermi levels (E_{fc}), respectively. E_{fc} values are also reported next to the CL spectra, along with the corresponding electron concentrations (n_{Efc}) determined using the non-parabolic band model, as shown in (f).

From the liquid Ga droplet seen on the SEM image of Te-NW1 (Figure 2a), the top of the NW can be easily distinguished from the bottom. Figure 2b shows the panchromatic CL intensity map of Te-NW1 from which an axial intensity gradient can be observed. We also note a blueshift and a broadening of the emission peak towards the top of the NW (Figure 2c and d), which is a signature of electron concentration gradient. In order to quantify the electron concentration, CL spectra are averaged over each of the 9 areas shown in Figure 2b (5 x 6 pixel^2 each, or 0.46 x 0.55 μm^2) and plotted in Figure 2e. The CL spectra are dominated by band-to-band recombination around 1.43 eV, although sub-bandgap emission is also observed and can be attributed to shallow defects. The main emission peak blueshifts and broadens from the bottom to the top of the NW (areas 1 to 9). It is fitted using the generalized Planck law and an absorption model using the method previously described for the thin film samples and detailed in references [27] and [30]. The fitted electron Fermi levels (squares in Figure 2e) are used to determine an electron concentration for values ranging from 1.6 x 10^{18} cm^{-3} (area 4) to 3.3 x 10^{18} cm^{-3} (area 9), see Figure 2f. At LT (Figure B1 in Appendix), although defect bands dominate the CL spectra, the same blueshift of the

GaAs CL peak can be observed from areas 1 to 9. The variations in FWHM are of the same order of magnitude as the RT FWHM values, from 104 meV to 135 meV, and they further confirm the gradient of electron concentration along the NW axis. Hence, this complete analysis shows that the axial electron concentration gradient in Te-NW1 can be determined at RT with a spatial resolution of 500 nm, corresponding here to the height of each of the 9 rectangular areas.

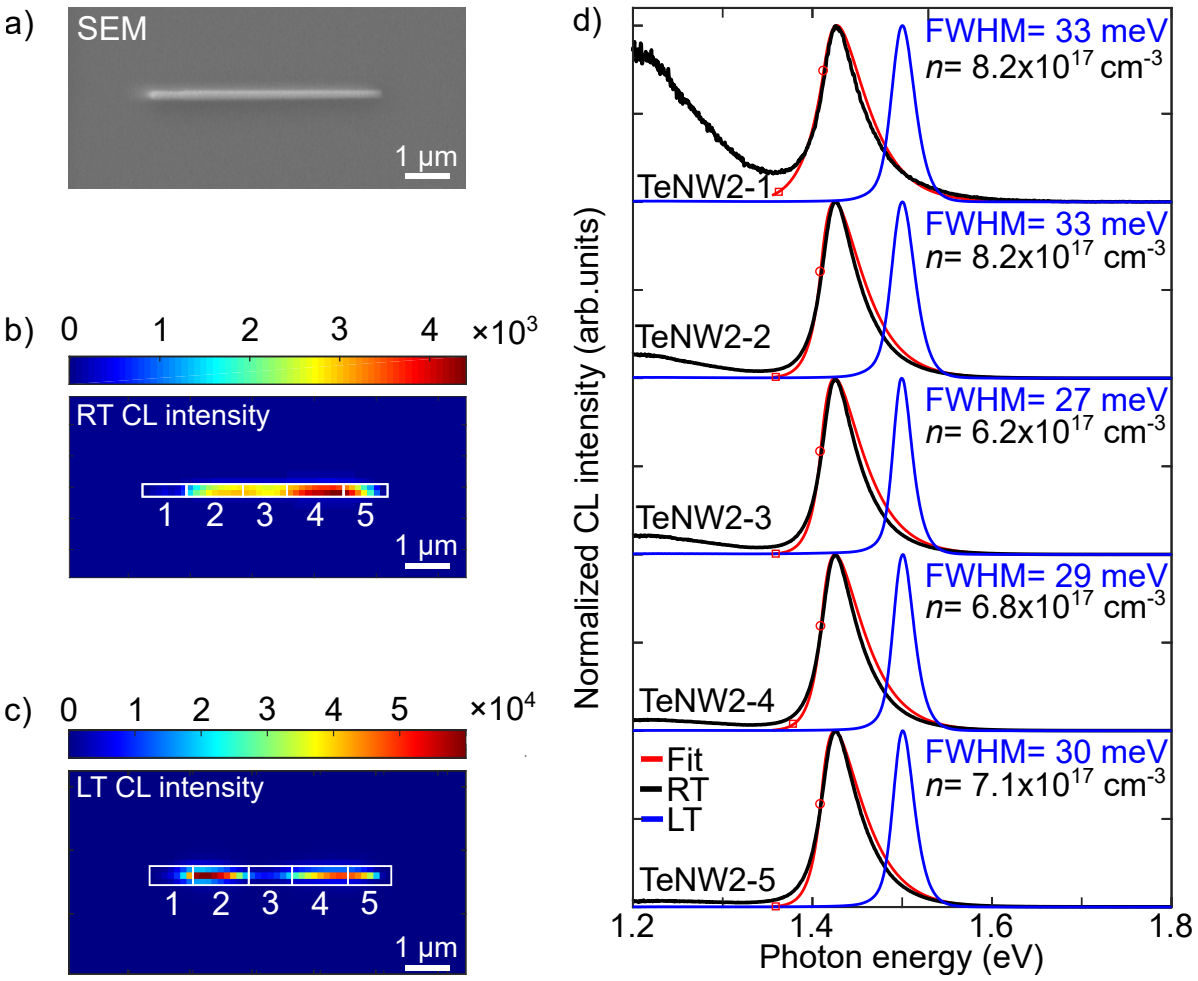

Figure 3. A single NW from sample Te-NW2 studied by RT and LT cathodoluminescence. (a) SEM, (b) RT and (c) LT panchromatic CL intensity maps (26 x 64 pixel^2 and 31 x 64 pixel^2 respectively for the intensity maps). RT (black) and LT (blue) CL spectra are extracted from the 5 areas shown in (b) and (c) (2-3 x 8-9 pixel^2) and plotted in (d). Red lines correspond to the fits of the RT CL spectra with the generalized Planck law, circles and squares indicate the fitted bandgaps (E_g= 1.41 eV) and electron Fermi levels ($E_{fc} < 0$), respectively. The electron concentrations (n) next to the spectra were obtained from the LT FWHM values indicated in blue, using the empirical model illustrated in Figure 1d.

4.2. NWs grown at 620 C (Te-NW2)

Sample Te-NW2 is grown at a temperature 20 C lower than Te-NW1 (620 C), and higher supersaturation in the Ga droplet resulted in longer and more tapered NWs. Figure 3a shows the SEM image of a single NW from Te-NW2, while Figure 3b and c present the RT and LT panchromatic CL intensity maps of this NW, respectively. At both RT and LT, the CL intensity is highest in areas 2 and 4, and lowest in areas 1 and 3, although the contrast between the different areas is more visible at LT. As seen from the TEM data in Figure A3 of the Appendix, Te-NW2 contains many defects arising from polytypism, stacking faults and twinning, which could act as non-radiative carrier recombination centres. The CL intensity variations may be the result of such bulk defects, but also depend on changes in the diffusion length and surface recombination. The CL maps suggest a higher density of such defects in areas 1 and 3. A slightly higher sub-bandgap emission is also observed in areas 1-3 (Figure 3d). The overall stronger CL intensity obtained from Te-NW2 compared to Te-NW1 can be understood by their different microstructures and dimensions. In order to quantify the carrier concentration in Te-NW2, an average RT CL spectrum is extracted from each of the 5 areas shown in Figure 3b (2 x 8-9 pixel^2 each, or 0.28 x 1 μm^2). These 5 RT CL spectra are then normalized by their maximum and plotted in Figure 3d (black curves). The similarities in CL peak energy and FWHM for all averaged RT CL spectra (corresponding CL maps in Figure B2 in Appendix) imply a relatively homogeneous axial electron concentration. This electron concentration could however not be quantified using the generalized Planck law method because the CL spectra could not be fitted accurately (red curve in Figure 3d, $E_{fc} < 0$), suggesting an electron concentration below 1 x 10^{18} cm^{-3}. The LT method based on the FWHM is then used to quantitatively determine the electron concentration in each of the 5 areas of Te-NW2 (3 x 8-9 pixel^2 each, or 0.41 x 1 μm^2). The FWHM values are extracted from each average LT CL spectra in Figure 3d (blue) and related to the electron concentrations according to Equation 1, as shown in Figure 1d (light blue region). The LT analysis confirms the homogeneous electron concentration along the NW axis with values between 6.2 x 10^{17} cm^{-3} and 8.2 x 10^{17} cm^{-3}.

4.3. Comparison

Figure 4 compares the electron concentrations determined in the two NW samples described above. The dotted lines serve as a guide to the eye to emphasize the inhomogeneous electron concentration in Te-NW1 as opposed to the homogeneous electron concentration in Te-NW2.

Generally, both Te-NW1 and Te-NW2 show around an order of magnitude lower electron concentration than the nominal dopant concentration calibrated by thin film growths. This is consistent with the previous reports on Te-incorporation in NW growth [13, 22]. The electron concentration gradient obtained for Te-NW1 is in good agreement with previous Raman spectroscopy results collected from the same sample [22], which indicated a carrier concentration of 1.2 x 10^{18} cm^{-3} at the bottom and of 4.1 x 10^{18}

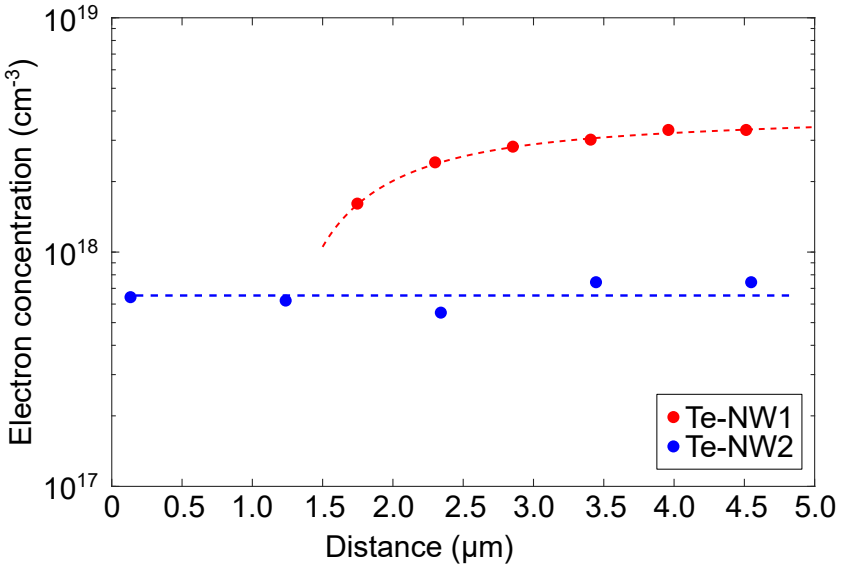

Figure 4. Spatial dependence of the electron concentration along the axis of the NW grown at 640 C (Te-NW1, red) and at 620 C (Te-NW2, blue). The bottom of the NW is at 0 μm. The dotted lines serve as guides to the eye.

cm^{-3} at the top of the NW. In contrast, Te-NW2 exhibits lower maximum doping than Te-NW1, with no carrier concentration gradient observed. As shown in reference [22], the primary incorporation mechanism of Te into self-catalysed GaAs NWs at a growth temperature of 640 °C is the vapor-liquid-solid mechanism through the Ga droplet. The Te incorporation via radial vapor-solid (VS) growth is inefficient at these high temperatures due to the high vapor pressure of Te [39]. The primary incorporation via droplet leads to both axial and radial dopant gradients. The droplet increases continuously in size as the NW grows. This forms an inversely tapered NW core which has grown in VLS mode and thus has higher doping. Simultaneously, VS growth on the NW sidewalls compensates the inverse tapering forming untapered NWs with a shell exhibiting lower doping. Hence, at the bottom of Te-NW1, only a thin core of the NW is doped via the VLS mechanism whereas the tip of Te-NW1 has grown fully via VLS growth. Te diffusion inside the NW mainly affects the radial gradients because of the high aspect ratio of the investigated NWs. Te-NW2 was grown at a lower temperature of 620 °C and thus an increase of VS incorporation efficiency via the sidewalls is expected. On the other hand, Te incorporation by the VLS process is reduced by differences in the kinetics and shape of the droplet. Te-NW2 NWs have a smaller droplet contact angle and were grown with a larger axial growth rate. Both of these features show that the droplets have exhibited higher As supersaturation during the NW growth. Since Te incorporates to As lattice sites [15], it is expected that the higher As supersaturation in the liquid phase weakens the Te incorporation via droplet. Simultaneously, the smaller effective droplet area for Te atom impingement in Te-NW2 reduces the collection rate of Te atoms from vapor phase to liquid phase when compared to Te-NW1. Therefore, the differences in the electron concentration levels and gradients between Te-NW1 and Te-

NW2 can be explained by different incorporation efficiencies by VLS and VS processes.

5. Conclusion

In this work cathodoluminescence is used to determine the electron concentration in Te-doped GaAs thin films and NWs. Measurements are first carried out on five GaAs:Te thin film references with electron concentrations between 5 x 10^{17} cm^{-3} and 1 x 10^{19} cm^{-3}. The correlation between cathodoluminescence spectrum and carrier concentration for GaAs:Te thin films is found to be consistent with previous work on GaAs:Si samples. This allows the extension of the carrier concentration assessment method previously developed for Si-doped GaAs at both room temperature and low temperature [27, 28, 30] to Te-doped GaAs. Mapping of the electron concentration in single NWs from two GaAs:Te NW samples is then carried out. Both Te-NW1 (grown at 640 C) and Te-NW2 (grown at 620 C) show an order of magnitude lower electron concentration than the nominal dopant concentration calibrated by thin film growths, in accordance with previous studies. An electron concentration gradient ranging from below 1 x 10^{18} cm^{-3} to 3.3 x 10^{18} cm^{-3} along the NW axis is determined for Te-NW1. In contrast, a homogeneous electron concentration of around 6 - 8 x 10^{17} cm^{-3} is observed along the NW axis of Te-NW2. The differences in the electron concentration levels and gradients between the two NW samples can be explained by different incorporation efficiencies via vapor-solid and vapor-liquid-solid processes. Overall, this study evidences that cathodoluminescence with nanoscale spatial resolution is a powerful technique to characterize the actual carrier concentration of single GaAs:Te NWs which can then be correlated to growth parameters (here the growth temperature). Such improvement in the assessment and control of impurity doping and hence properties in NWs will undoubtedly help pave the way to the design of next-generation electronic devices.

Acknowledgments

CT, TB, AC and SC acknowledge financial support from the French government for this project in the frame of the Programme dInvestissement dAvenir - ANR-IEED-002-01 and the ANR projects Nanocell (ANR-15-CE05-0026) and Hetonan (ANR-15-CE05-0009). This work was also partly funded in the frame of the EMPIR 19ENG05 NanoWires project. The EMPIR (European Metrology Programme for Innovation and Research) initiative is co-funded by the European Unions Horizon 2020 research and innovation programme and the EMPIR Participating States. EK, MG, and TH acknowledge financial support from the Academy of Finland Projects QuantSi (Decision No. 323989) and NanoLight (Decision No. 310985). YGG and HVAG acknowledge the Fundao de Amparo a Pesquisa do Estado de So Paulo (Fapesp) (grants 19/23488-5, 19/07442-5 and 14/50513-7).

Appendix A. Electron microscopy observations of Te-NW1 and Te-NW2.

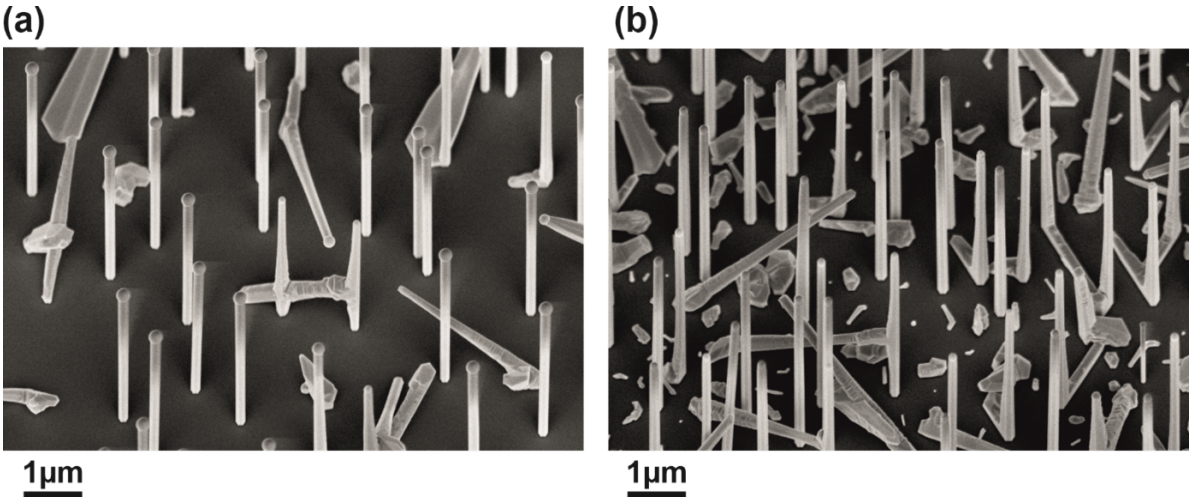

Figure A1. Tilted view (30) SEM pictures of (a) Te-NW1 and (b) Te-NW2.

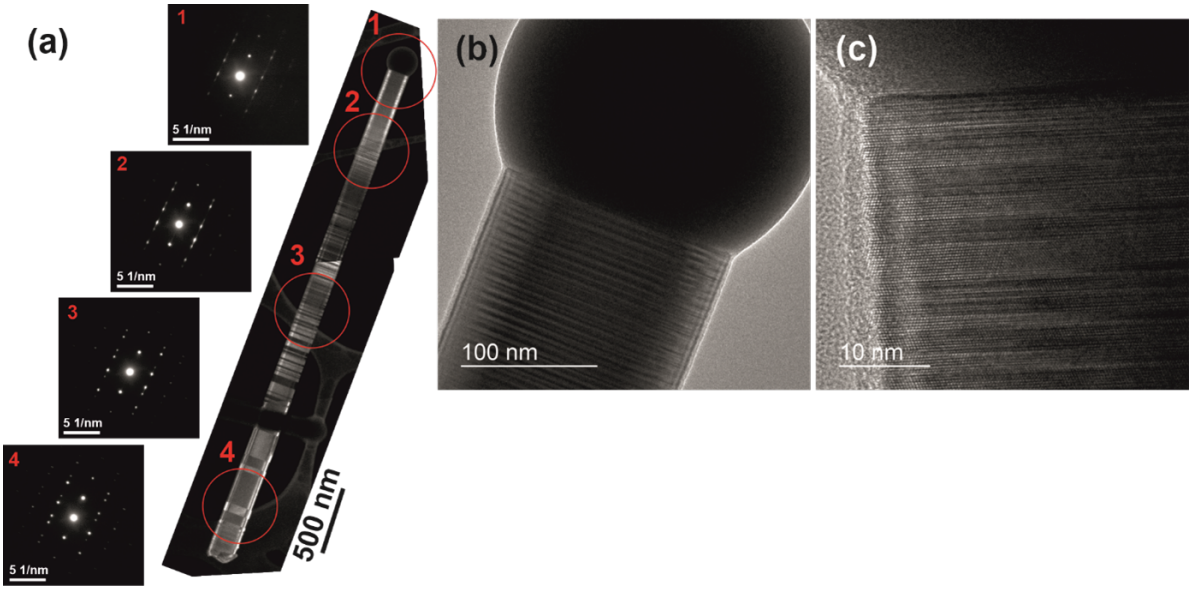

Figure A2. TEM data for Te-NW1. (a) HR-TEM overview and selected-area diffraction patterns measured from four different areas along the NW showing twinned zinc blende crystal structure with frequent twinning. (b) and (c) show high-resolution HR-TEM micrographs from area 1.

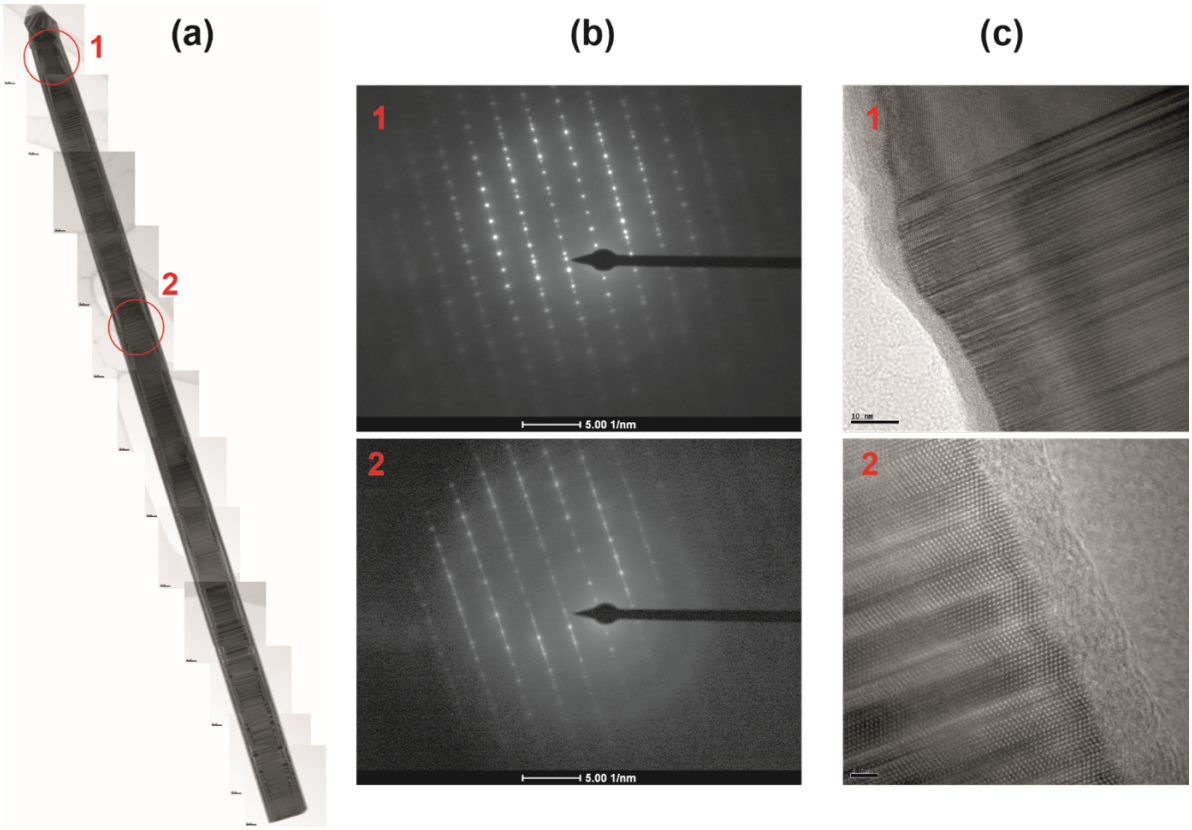

Figure A3. TEM data for Te-NW2. (a) HR-TEM overview of the NW. (b) Selected-area diffraction patterns from two different locations along the NW show polytypism, stacking faults and twinning. (c) High-resolution HR-TEM micrographs from areas 1 and 2.

Appendix B. Complementary CL results on Te-NW1 and Te-NW2.

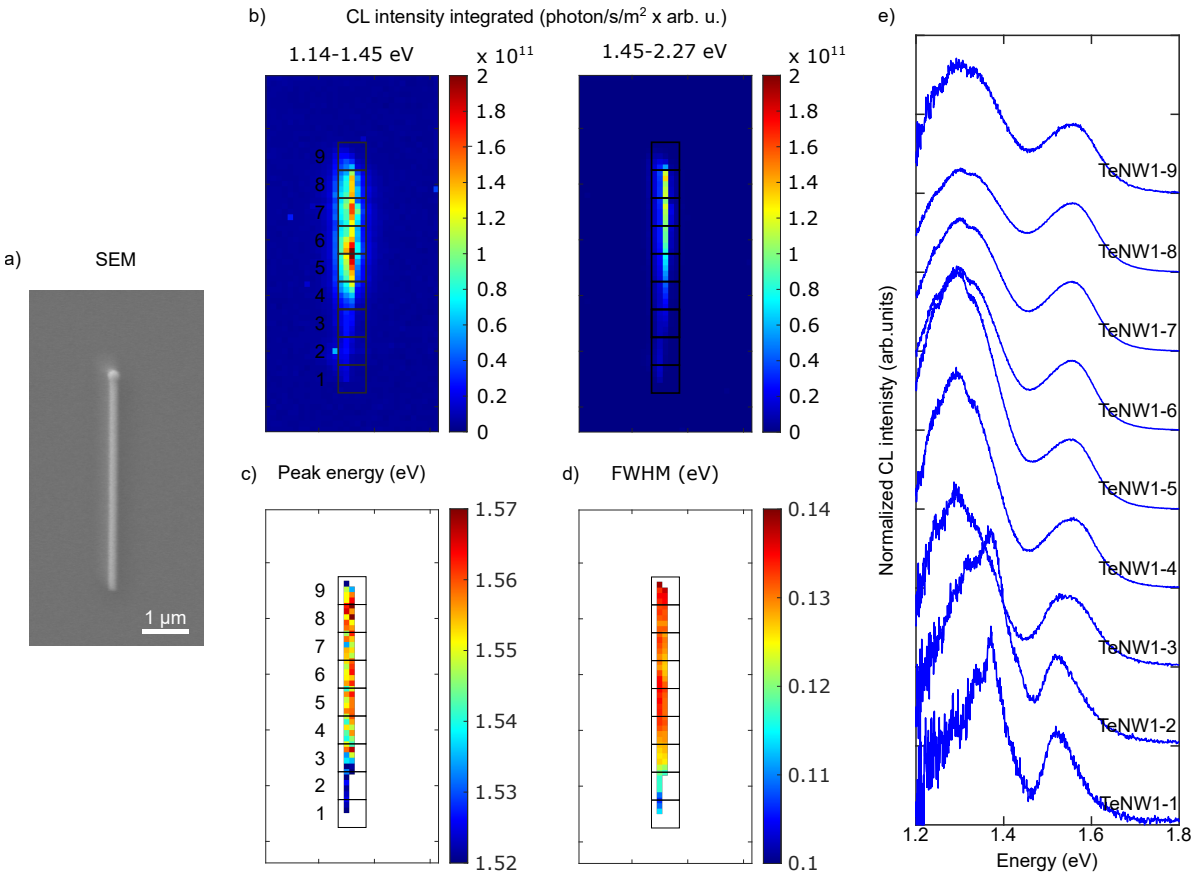

Figure B1. (a) SEM image of the NW from Figure 2 (Te-NW1) and its corresponding maps measured at LT: (b) CL intensity maps integrated between 1.14 - 1.45 eV (left) and 1.45 - 2.27 eV (right), (c) CL peak energy and (d) FWHM (31 x 64 pixel^2). The 9 areas indicated (5 x 6 pixel^2 each) correspond to the areas over which the CL spectra in (e) are averaged.

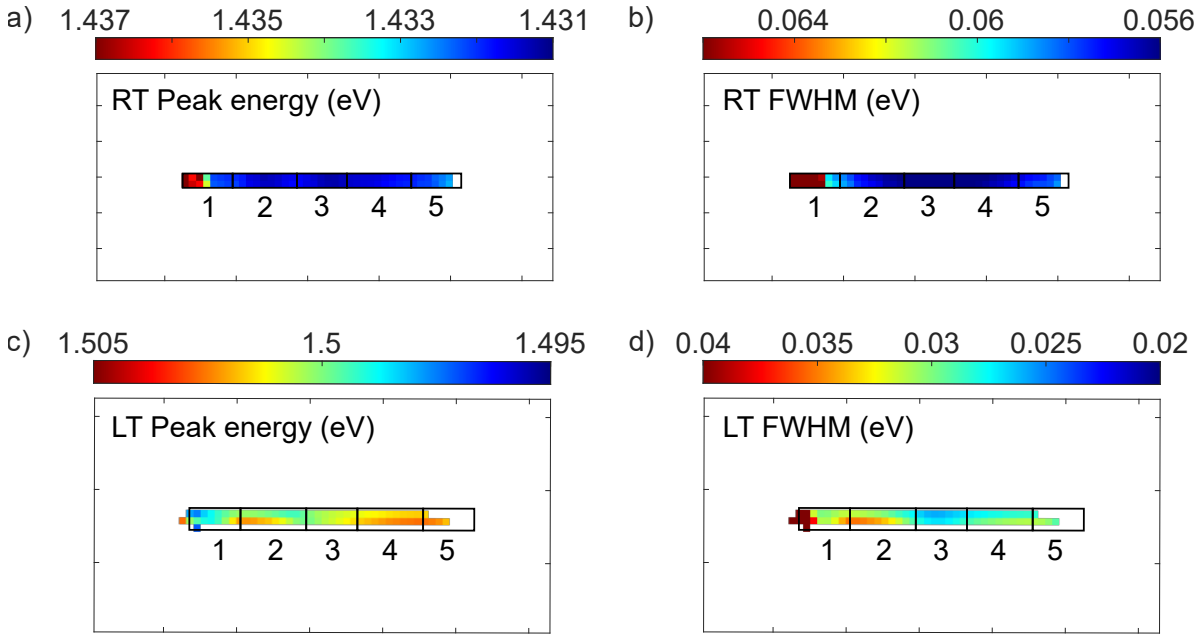

Figure B2. Te-NW2 RT maps of (a) CL peak energy and (b) FWHM (29 x 64 pixel^2), as well as LT maps of (c) CL peak energy and (d) FWHM (32 x 64 pixel^2). The 5 areas indicated (2-3 x 8-9 pixel^2) correspond to the areas over which the CL spectra from Figure 3 are averaged.

References

[1] Wei Lu, Ping Xie, and Charles M. Lieber. Nanowire transistor performance limits and applications. *IEEE Transactions on Electron Devices*, 55(11):2859–2876, 2008.

[2] Ziyuan Li, Jeffery Allen, Monica Allen, Hark Hoe Tan, Chennupati Jagadish, and Lan Fu. Review on III-V semiconductor single nanowire-based room temperature infrared photodetectors. *Materials*, 13(6):1400, 2020.

[3] Nan Guan, Xing Dai, Andrey Babichev, Franois Julien, and Maria Tchernycheva. Flexible inorganic light emitting diodes based on semiconductor nanowires. *Chemical Science, The Royal Society of Chemistry*, 8(12):7904–7911, 2017.

[4] Yunyan Zhang and Huiyun Liu. Nanowires for high-efficiency, low-cost solar photovoltaics. *Crystals*, 9(2):87, 2019.

[5] Jie Xiang Wei Lu. *Semiconductor Nanowires: From Next-Generation Electronics to Sustainable Energy*, volume 39. The Royal Society of Chemistry, 2015.

[6] Andrew C.E. Chia and Ray R. Lapierre. Analytical model of surface depletion in GaAs nanowires. *Journal of Applied Physics*, 112(6):063705, 2012.

[7] Wonjong Kim, Lucas Güniat, Anna Fontcuberta I Morral, and Valerio Piazza. Doping challenges and pathways to industrial scalability of III-V nanowire arrays. *Applied Physics Reviews*, 8(1):011304, 2021.

[8] R. S. Wagner and W. C. Ellis. Vapor-liquid-solid mechanism of single crystal growth. *Applied Physics Letters*, 4(5):89–90, 1964.

[9] R. R. Lapierre, A. C.E. Chia, S. J. Gibson, C. M. Haapamaki, J. Boulanger, R. Yee, P. Kuyanov, J. Zhang, N. Tajik, N. Jewell, and K. M.A. Rahman. III-V nanowire photovoltaics: Review of design for high efficiency. *Physica Status Solidi - Rapid Research Letters*, 7(10):815–830, 2013.

[10] M. H. T. Dastjerdi, E M Fiordaliso, E D Leshchenko, A Akhtari-Zavareh, T Kasama, M Aagesen, V G Dubrovskii, and R R LaPierre. Three-fold Symmetric Doping Mechanism in GaAs

Nanowires. *Nano Letters*, 17(10):5875–5882, 10 2017.

[11] N. Isik Goktas, P Wilson, A Ghukasyan, D Wagner, S McNamee, and R. R. Lapierre. Nanowires for energy : A review. *Applied Physics Reviews*, 5(4):041305, 2018.

[12] Marcelo Rizzo Piton, Teemu Hakkarainen, Joonas Hilska, Eero Koivusalo, Donald Lupo, Helder Vinicius Avano Galeti, Yara Galvão Gobato, and Mircea Guina. Optimization of Ohmic Contacts to p-GaAs Nanowires. *Nanoscale Research Letters*, 14(344), 2019.

[13] Vladimir G. Dubrovskii, Hadi Hijazi, Nebile Isik Goktas, and Ray R. Lapierre. Be, Te, and Si Doping of GaAs Nanowires: Theory and Experiment. *Journal of Physical Chemistry C*, 124(31):17299–17307, 2020.

[14] A. Y. Cho. *Growth and Properties of III-V Semiconductors By Molecular Beam Epitaxy and Their Properties*, volume 100. Elsevier Sequoi, 1983.

[15] E. Fred Schubert. *Doping in III-V Semiconductors*. Cambridge University Press, 1993.

[16] C. Colombo, M. Heiß, M. Grätzel, and A. Fontcuberta I Morral. Gallium arsenide p-i-n radial structures for photovoltaic applications. *Applied Physics Letters*, 94(17):13–16, 2009.

[17] M Hilse, M Ramsteiner, S Breuer, L Geelhaar, and H Riechert. Incorporation of the dopants Si and Be into GaAs nanowires. *Applied Physics Letters*, 96(19):193104, 2010.

[18] Hadi Hijazi, Guillaume Monier, Evelyne Gil, Agns Trassoudaine, Catherine Bougerol, Christine Leroux, Dominique Castellucci, Christine Robert-Goumet, Philip E. Hoggan, Yamina André, Nebile Isik Goktas, Ray R. Lapierre, and Vladimir G. Dubrovskii. Si doping of vapor-liquid-solid gaas nanowires: N-Type or p-Type? *Nano Letters*, 19(7):4498–4504, 2019.

[19] S. Suomalainen, T. V. Hakkarainen, T. Salminen, R. Koskinen, M. Honkanen, E. Luna, and Mircea Guina. Te-doping of self-catalyzed GaAs nanowires. *Applied Physics Letters*, 107(1):1–5, 2015.

[20] N. Isik Goktas, E. M. Fiordaliso, and R R LaPierre. Doping assessment in GaAs nanowires. *Nanotechnology*, 29(23):234001, 2018.

[21] Marta Orrù, Eva Repiso, Stefania Carapezzi, Alex Henning, Stefano Roddaro, Alfonso Franciosi, Yossi Rosenwaks, Anna Cavallini, Faustino Martelli, and Silvia Rubini. A Roadmap for Controlled and Efficient n-Type Doping of Self-Assisted GaAs Nanowires Grown by Molecular Beam Epitaxy. *Advanced Functional Materials*, 26(17):2836–2845, 2016.

[22] Teemu Hakkarainen, Marcelo Rizzo Piton, Elisabetta Maria Fiordaliso, Egor D Leshchenko, Sebastian Koelling, Jefferson Bettini, Helder Vinicius, Avano Galeti, Eero Koivusalo, Yara Galvo Gobato, Ariano De Giovanni Rodrigues, Donald Lupo, Paul M Koenraad, Edson Roberto Leite, Vladimir G Dubrovskii, and Mircea Guina. Te incorporation and activation as n -type dopant in self-catalyzed GaAs nanowires. *Physical Review Materials*, 3(8):086001, 2019.

[23] Priyanka Ramaswamy, Shisir Devkota, Rabin Pokharel, Surya Nalamati, Fred Stevie, Keith Jones, Lew Reynolds, and Shanthi Iyer. A study of dopant incorporation in Te-doped GaAsSb nanowires using a combination of XPS/UPS, and C-AFM/SKPM. *Scientific Reports*, 11(1):1–14, 2021.

[24] Kristian Storm, Filip Halvardsson, Magnus Heurlin, David Lindgren, Anders Gustafsson, Phillip M Wu, Bo Monemar, and Lars Samuelson. Spatially resolved Hall effect measurement in a single semiconductor nanowire. *Nature Nanotechnology*, 7:718–722, 2012.

[25] David Lindgren, Olof Hultin, Magnus Heurlin, Kristian Storm, Magnus T. Borgström, Lars Samuelson, and Anders Gustafsson. Study of carrier concentration in single InP nanowires by luminescence and Hall measurements. *Nanotechnology*, 26(4):045705, 2015.

[26] Valerio Piazza, Lorenzo Mancini, Hung Ling Chen, Stphane Collin, and Maria Tchernycheva. Nanoscale Analyses Applied to Nanowire Devices. In *Semiconductors and Semimetals*, volume 98, chapter 4, pages 231–319. Academic Press, 2018.

[27] Hung Ling Chen, Andrea Scaccabarozzi, Romaric De Lepinau, Fabrice Oehler, Aristide Lemaitre, Jean Christophe Harmand, Andrea Cattoni, and Stephane Collin. Quantitative Assessment of Carrier Density by Cathodoluminescence. I. GaAs Thin Films and Modeling. *Physical Review Applied*, 15(2):024006, 2021.

[28] Hung Ling Chen, Romaric De Lépinau, Andrea Scaccabarozzi, Fabrice Oehler, Jean Christophe

Harmand, Andrea Cattoni, and Stphane Collin. Quantitative Assessment of Carrier Density by Cathodoluminescence. II. GaAs nanowires. *Physical Review Applied*, 15(2):024007, 2021.

[29] T. V. Hakkarainen, A. Schramm, J. Mäkelä, P. Laukkanen, and M. Guina. Lithography-free oxide patterns as templates for self-catalyzed growth of highly uniform GaAs nanowires on Si(111). *Nanotechnology*, 26(27):275301, 2015.

[30] Hung-Ling Chen, Chalemchai Himwas, Andrea Scaccabarozzi, Pierre Rale, Fabrice Oehler, ARtiside Lemaitre, Laurent Lombez, Jean-Francois Guillemoles, Maria Tchernycheva, Jean-Christophe Harmand, Andrea Cattoni, and Stephane Collin. Determination of nType Doping Level in Single GaAs Nanowires by Cathodoluminescence. *Nano Letters*, 17:6667–6675, 2017.

[31] Eero S. Koivusalo, Teemu V. Hakkarainen, Mircea D. Guina, and Vladimir G. Dubrovskii. Sub-Poissonian Narrowing of Length Distributions Realized in Ga-Catalyzed GaAs Nanowires. *Nano Letters*, 17(9):5350–5355, 2017.

[32] J. S. Blakemore. Semiconducting and other major properties of gallium arsenide. *Journal of Applied Physics*, 53(10):123–181, 1982.

[33] Nam Young Lee, Kyu Jang Lee, Chul Lee, Jae Eun Kim, Hae Yong Park, Dong Hwa Kwak, Hee Chul Lee, and H. Lim. Determination of conduction band tail and fermi energy of heavily Si-doped GaAs by room-temperature photoluminescence. *Journal of Applied Physics*, 78(5):3367–3370, 1995.

[34] Elias Burstein. Anomalous optical absorption limit in InSb [4]. *Physical Review*, 93(3):632–633, 1954.

[35] T. S. Moss. The interpretation of the properties of indium antimonide. *Proceedings of the Physical Society. Section B*, 67(10):775–782, 1954.

[36] Jiang De-Sheng, Y. Makita, K. Ploog, and H. J. Queisser. Electrical properties and photoluminescence of Te-doped GaAs grown by molecular beam epitaxy. *Journal of Applied Physics*, 53(2):999–1006, 1982.

[37] A. Raymond, J. L. Robert, and C. Bernard. The electron effective mass in heavily doped GaAs. *Journal of Physics C: Solid State Physics*, 12(12):2289–2293, 1979.

[38] Federico Panciera, Zhaslan Baraissov, Gilles Patriarche, G Vladimir, Frank Glas, Laurent Travers, Utkur Mirsaidov, Jean Christophe, Federico Panciera, Zhaslan Baraissov, Gilles Patriarche, Vladimir G Dubrovskii, and Frank Glas. Phase Selection in Self-catalyzed GaAs Nanowires. *Nano Letters*, 20:1669–1675, 2020.

[39] Douglas M. Collins, J. N. Miller, Young G. Chai, and Robert Chow. Sn and Te doping of molecular beam epitaxial GaAs using a SnTe source. *Journal of Applied Physics*, 53(4):3010–3018, 1982.